J Mater Sci **(2022) 57:2839–2856**

Energy materials

$Ni/Ce_xZr_{1-x}O_2$ catalyst prepared via one-step co-precipitation for CO_2 reforming of CH_4 to produce syngas: role of oxygen storage capacity (OSC) and oxygen vacancy formation energy (OVFE)

Manohar Prasad[1], Koustuv Ray[2], Apurba Sinhamahapatra[1,*], and Siddhartha Sengupta[1,*]

[1] Department of Chemical Engineering, Indian Institute of Technology (Indian School of Mines) Dhanbad, Dhanbad 826004, India
[2] Department of Chemical Engineering, Indian Institute of Technology Kharagpur, Kharagpur 721302, India

Received: 23 August 2021
Accepted: 12 November 2021

ABSTRACT

Ceria-zirconia solid solution ($Ce_{0.5}Zr_{0.5}O_2$)-supported Ni catalyst (15 wt. %) is prepared by one-step co-precipitation followed by calcination reduction for CO_2 reforming of CH_4 (DRM). Oxygen storage capacity (OSC) is measured by O_2 pulse injection at the reaction temperature. The solid solution is formed upon incorporating Zr^{4+} into ceria, subsequently accelerating oxygen mobility from lattice (bulk) to the surface, enhancing $\%Ce^{3+}$ due to increased oxygen vacancies, and thus improving OSC, reducibility, surface basicity, and Ni dispersion compared to pure CeO_2 and ZrO_2. The solid solution exhibits better conversions of CH_4 and CO_2, a higher H_2/CO ratio, and low carbon deposition compared to its pure counterpart. The density functional theory (DFT) studies unveil oxygen vacancy formation energy (OVFE) as a descriptor that decreased for $Ce_{0.5}Zr_{0.5}O_2$ due to the incorporation of Zr^{4+} and enhanced mobility of O anions, OSC, and reducibility.

Introduction

Oxygen storage capacity (OSC) is the ability of a material to exchange its lattice oxygen for redox reactions under suitable operating conditions due to low redox potential [1, 2]. A catalyst with higher OSC can be efficiently used in several industrially important reactions such as reforming, water–gas shift, catalytic conversion of pollutants, dehydration of alcohols, fine chemicals production, photocatalysis, etc. [1, 3, 4]. In this context, the application of higher OSC materials in dry reforming of methane (DRM), which converts CO_2 and CH_4 into syngas, has gained significant attention [5, 6]. The high OSC helps to diminish the carbon deposition during the highly

---

Handling Editor: Till Froemling.

Address correspondence to E-mail: apurba@iitism.ac.in; siddhartha@iitism.ac.in

https://doi.org/10.1007/s10853-021-06720-5

endothermic reaction of DRM. Deposited carbonaceous species cause severe catalyst deactivation [7, 8]. In this context, ceria (CeO_2)-based catalysts attracted attention over the last few years due to their high OSC associated with rich oxygen vacancies, which arises from low redox potential between Ce^{3+} and Ce^{4+} [2, 6]. However, at higher temperatures (> 623 K), pure ceria suffers from limited OSC and poor thermal stability due to sintering and subsequent decrease in the surface area [9, 10]. Modification of pure ceria's properties by incorporating suitable isovalent dopants like Zr^{4+}, Hf^{4+}, Si^{4+}, Tb^{4+}, Pr^{4+}, Ti^{4+}, Sn^{4+}, $Mn^{2+}/^{3+}$, $Fe^{2+}/^{3+}$, and aliovalent dopants such as La^{3+} (Sm^{3+}, Eu^{3+}, $Tb^{3+/4+}$, $Pr^{3+/4+}$) is explored [2, 4]. Incorporating Zr^{4+} into ceria to form the ceria-zirconia (CZ) solid solution ($Ce_xZr_{1-x}O_2$) is one of the most promising approaches to enhance OSC, redox properties, and basic properties [6, 8]. It has also been observed that solid solution is beneficial for smaller catalyst size, increased metal dispersion, improved structural stability, and enhanced catalytic performances [1, 3, 6].

Catalyst preparation techniques play a vital role in catalytic performances. Methods like hydrothermal, solvothermal, surfactant-assisted, sol-gel, solution combustion, mechanical mixing, and co-precipitation are used to prepare $Ce_xZr_{1-x}O_2$ [11–13]. The co-precipitation method offers higher homogeneity, enhanced surface area, smaller catalyst size, and improved OSC leading to higher catalytic performances [14, 15]. It is also observed that the co-precipitation method provides improved thermal stability and a strong interaction between metal catalyst and support [11, 13, 16, 17]. Studies are available to synthesize CZ supports via the co-precipitation method, however different techniques are employed for metal loading. This technique often leads to inhomogeneous metal distribution and poor metal–support interaction, causing metal agglomeration at high temperatures leading to loss of catalytic activity. In this context, one-step co-precipitation of metal and support could be a desirable approach for metal-supported CZ catalyst for DRM, which is rarely reported.

Incidentally, previous studies quantitatively related the unique properties of $Ce_xZr_{1-x}O_2$ solid solutions, i.e., OSC with oxygen vacancy formation energy (OVFE) [18–21]. OVFE determines whether one or more vacant oxygen sites can be created, which renders the structure capable of storing or releasing oxygen atoms during a catalytic cycle. The addition of dopants such as Pd, Pt, and Zr into the CeO_2 lattice has effects on lowering the oxygen vacancy formation energy, thereby creating vacant sites more favorably than pure CeO_2 [20, 22–24]. The effects on either bulk or surface structure are the result of various factors such as the type of dopant, the concentration of dopant, and the location of the oxygen vacancy site. In the last few years, density functional theory (DFT) calculations have emerged to shed more insights on OVFE and estimate quantitatively the same [18, 19, 25]. However, available studies investigated OVFE either for very low concentration of zirconia for the bulk structure of (2 × 2 × 2), or various concentrations of zirconia for the bulk structures of (1 × 1 × 1) and (1 × 2 × 1) only at very high Monkhorst-Pack *k* point (6 × 6 × 6) [18, 19, 21, 25]. The OSC of CeO_2 plays an important role in the redox reaction and facilitates catalysis by favorable adsorption and activation of the key reactant molecule; therefore, it is necessary to understand such rationale behind the DRM reaction. Therefore, it is desirable to develop correlations involving OSC, OVFE, catalytic activity, and deactivation of the ceria-zirconia solid solution for improved understanding. This development will eventually be helpful for the design of CZ-supported catalysts for large-scale applications.

Herein, supports (ceria, ceria-zirconia, and zirconia) and Ni-supported catalysts were synthesized via the one-step co-precipitation method for DRM reaction. The OSC of the support was measured by the oxygen pulse injection method at the DRM reaction temperature. Traditionally, various techniques like thermogravimetric analysis (TGA), temperature-programmed reduction/temperature-programmed oxidation (TPR/TPO), O_2-chemisorption, CO/H_2 pulse injection, and magnetic susceptibility measurement methods are employed to measure OSC quantitatively, based on the reduction of oxides by molecular H_2/CO and re-oxidation by molecular O_2 [2, 15, 26]. It is observed that measured OSC is affected by the concentration of H_2/CO and the presence of H_2O and CO_2 produced during measurement [2, 27]. Additionally, it is observed that the OSC is often measured at a lower temperature [2, 12, 15, 17], which may not provide the exact OSC available at a higher reaction temperature. Hence, it appears to be desirable to perform an OSC measurement experiment at the reaction temperature. Further, temperature-programmed hydrogenation (TPH) studies are also carried out to understand the source of carbon formation during the DRM reaction. Finally, DFT calculations are performed on the (2 × 2 × 2) bulk structure of pure ceria, zirconia, and one CZ oxide by introducing Zr into the ceria lattice at a particular Ce/Zr ratio to obtain relaxed cell parameters, interatomic distances, and the OVFE. The computational results were correlated with our experimental observations to provide an improved understanding of DRM catalysis.

Experimental

Catalysts synthesis

CeO_2, ZrO_2, and $Ce_{0.5}Zr_{0.5}O_2$ were prepared by the co-precipitation method using aqueous 1N NaOH as a precipitating agent. In a typical process, the required amount of Ce $(NO_3)_3·6H_2O$ (Sigma-Aldrich, 99.9%) and ZrO $(NO_3)_2·6H_2O$ (Sigma-Aldrich, 99%) were dissolved in 50 ml deionized water. Aqueous NaOH was added drop-wise to the freshly prepared solution for precipitation, and pH was adjusted to ~ 9. Then, the precipitate was kept at room temperature for aging with continuous stirring at 350 rpm for 5 h. After aging, the residue was washed with distilled water several times to remove nitrates and other impurities. Finally, the obtained precipitate was dried at 373 K for 24 h, followed by calcination at 823 K for 5 h in air.

A similar procedure was followed to synthesize NiO-loaded CeO_2, ZrO_2, and $Ce_{0.5}Zr_{0.5}O_2$ using Ni $(NO_3)_2·6H_2O$ (Sigma Aldrich, 99.9%). The materials were further reduced in H_2 at 823 K for 2 h to obtain Ni-loaded CeO_2, ZrO_2, and $Ce_{0.5}Zr_{0.5}O_2$. Total metal loading was 15 wt.% concerning each support.

Characterizations

The powder X-ray diffraction (XRD) patterns were measured by using a Bruker D-8 advance diffractometer. The $2\theta = 20^\circ - 80^\circ$ was recorded using Cu Kα x-ray radiation with a step size of 0.05°/h. The Debye–Scherer equation was used to calculate the average crystallite size (D).

Raman spectroscopy measurements were performed using a LabRAM HR Evolution Raman Spectrometer (Horiba Scientific, Japan) with a 532 nm laser source.

The X-ray photoelectron spectra (XPS) were recorded with PHI 5000 versa probe III using a standard X-ray source with Al mono (24.1 W, 100 μ, 318 K, and 280 eV).

The morphology, particle size distribution, scanning transmission electron microscopy (STEM), elemental mapping, and energy-dispersive X-ray spectroscopy (EDS) analysis of catalysts were measured using High-Resolution Transmission Electron Microscope (HRTEM), Talos F200X G2 (Thermo scientific).

The OSC was calculated using the O_2 pulse injection experiment in catalyst characterization equipment BELCAT II, Japan. The total amount of O_2 uptake was equal to the total OSC [2]. In a typical procedure, the sample was heated to 873 K in 20% O_2/He, and then the sample was cooled to 323 K, followed by purging with He for 0.5 h. Then, the sample was reduced under 10% H_2/Ar at varying temperatures (323–873 K), followed by purging by He for 0.5 h. After that, O_2 pulse was injected every 0.033 h at 873 K, and O_2 uptake was measured till saturation.

Hydrogen temperature-programmed reduction (H_2-TPR) was used to determine the reducibility of the sample in BELCAT II. Approximately 0.030 g of sample was calcined at 823 K in 5% O_2/He for 1 h and cooled to 323 K in He. Then, the H_2-TPR profile was obtained using 10% H_2/Ar at a variable temperature ranging from 323 to 880 K with a hold time of 0.33 h. The amount of H_2 consumed is assumed to be equal to the amount of NiO reduced [7].

Hydrogen temperature-programmed desorption (H_2-TPD) was used to find the number of surface-active metal sites using BELCAT II. The number of surface-active metal sites was calculated based on H_2 chemisorption, assuming stoichiometry ratio of $H_2/Ni_{\text{active site}} = 1$ [28]. Before measuring H_2-TPD, about 0.05 g of sample was reduced at 823 K and cooled to 323 K. To obtain the H_2-TPD profile, temperature was increased (0.167 K h^{-1}) from 323 to 800 K in Ar.

Carbon dioxide temperature-programmed desorption (CO_2-TPD) was carried out using BELCAT II to estimate the basicity of the samples. The sample (0.05 g) was reduced at 823 K and cooled to 323 K, followed by He flushing for 0.5 h. Then, CO_2 was allowed to flow at a gas hourly space velocity (GHSV) of 60,000 ml g^{-1} h^{-1} for 0.5 h, followed by He flushing for 0.5 h. Finally, the CO_2-TPD profile was recorded at a temperature ranging from 323 to 800 K with a heating rate of 0.167 K h^{-1} in He.

Dry reforming of methane (DRM)

The catalytic DRM was performed in a down-flow fixed bed reactor (id 15.75 mm and 300 mm length) of INC 800, supplied by Chemito, India, enclosed in a half split-type tubular furnace made of stainless steel equipped with a PID temperature controller. The catalyst bed was placed on quartz wool, which was made at the center of the reactor. A mixture of NiO-loaded catalyst and quartz particles (used as diluents) was taken to form a bed height of about 0.01 m to prevent gas channeling within the catalyst bed. An in situ reduction step was performed before the reaction to convert NiO to Ni. The reactor's temperature was measured by a thermocouple located above the catalyst bed, controlled by a PID temperature controller, and sustained at 873 K throughout the reaction. The flow rates of all the reactants: CO_2, CH_4, and N_2, were controlled by separate mass flow controllers, and the volumetric ratio of $CH_4/CO_2/N_2$ was kept at 1: 1: 3. N_2 was used as an inert to control the mass and heat transfer effects, and GHSV = 60,000 ml g^{-1} h^{-1} was maintained. The catalyst was reduced in situ with H_2 at 823 K for 2 h to obtain the active form. The gaseous products were studied using a gas chromatograph (GC) (MICHO 9100, Netel, India) equipped with an SS column (3.2 mm o.d. × 1.8 m long) packed with a carbosphere (80–100 mesh). The reaction was monitored at a periodic interval of 0.5 h for the duration of 4 h. The conversions and H_2/CO ratio were calculated from the GC results using the formulae found elsewhere [29, 30].

The turnover frequency (TOF) was estimated based on CH_4 conversion and surface-active metal sites from H_2-TPD result using the formulae [29, 30]:

$$\mathrm{TOF}\left(s^{-1}\right) = \frac{\mathrm{CH_4\ flow\ rate\ (mol/s)}}{\mathrm{wt.\ of\ cat.}(\mathrm{g})} \times \frac{\mathrm{CH_4\ conversion\ (\%\ )}}{100} \times \frac{1}{M_s(\mathrm{mol/g})}$$

Carbon deposition study

CH_4 cracking to CH_x(x = 0–3) species is a vital step for the DRM reaction, and it is one of the crucial sources of carbon along with Boudouard (CO disproportionation) reaction on the supported Ni-based catalysts [31]. Temperature-programmed hydrogenation (TPH) was studied using BELCAT II to analyze the nature of carbon deposited on the catalysts after CO_2, CH_4 cracking and DRM reaction at 873 K. Before the measurement, 0.02 g of pre-reduced sample was reduced again (in situ) for 0.5 h in 10% H_2/Ar followed by flushing with Ar for 0.17 h and temperature was increased to 873 K. After that, two different techniques were performed to investigate the deposited carbon species.

a) At 873 K, CO_2 and CH_4 were treated separately for 0.17 h using 20% CO_2/Ar and 20% CH_4 (GHSV = 60,000 ml g^{-1} h^{-1}), respectively, followed by purging with Ar and cooled to 323 K. Then, the sample was heated to 1173 K with a heating rate of 0.167 K h^{-1} in 10% H_2/Ar.
b) At 873 K, a reaction was performed to replicate the DRM for 0.17 h using a volumetric ratio of $CH_4/CO_2/Ar$ = 1:1:3; a similar gaseous feed was used for DRM reaction. Then, the sample was treated with a stream of Ar and cooled to 323 K. The temperature was increased to 1173 K with a heating rate of 0.167 K h^{-1} in 10% H_2/Ar. The experiment is denoted as replicated DRM (r-DRM).

The H_2 uptake during the TPH experiment was measured, and the obtained profiles were compared.

Measurement of total deposited carbon

The amount of deposited carbon after 4 h was determined by elemental analysis of spent catalyst using a CHNSO Element analyzer (Vario, Elementar).

Density functional theory calculations

The generalized gradient approximation (GGA) and Perdew-Wang 1991 (PW91) exchange–correlation functional were used to relax the bulk structure under the DFT formalism using the CASTEP code [32–34]. The cutoff energy of 540 eV was chosen following the typical procedure of input parameter optimization. The calculations were made using a supercell (2 × 2 × 2) to keep the defect–defect interactions small and accurately estimate the oxygen vacancy formation energy of the bulk structure [25]. The convergence threshold was set to 1.0 × 10^{-6} eV/

atom for a self-consistent field (SCF), 5.0×10^{-6} eV/atom for energy, 0.02 eV/Å for maximum force, and 2.0×10^{-3} Å for maximum displacement. The self-consistent electron density was obtained by iterative diagonalization of the Kohn–Sham Hamiltonian, and the occupation of the Kohn-Sham states was smeared according to the Fermi–Dirac distribution with a smearing factor of $k_BT = 0.05$ eV [35]. The effect of spin polarization was not considered in this study.

The oxygen vacancy formation energy (E_v^f expressed in eV) was calculated according to the following formulae:

$$E_v^f = E(Ce_xZr_{1-x}O_{2-\delta}) + \frac{1}{2}E(O_2) - E(Ce_xZr_{1-x}O_2)-$$

where $E(Ce_xZr_{1-x}O_2)$ and $E(Ce_xZr_{1-x}O_{2-\delta})$ are the total energy of optimized bulk structure and optimized defect bulk structure (due to an oxygen vacancy) and $E(O_2)$ is gas-phase energy of an oxygen molecule [18, 19].

Results and discussion

Structural and morphological analysis

The powder XRD pattern of the prepared samples was recorded, and the results are presented in Fig. 1. The XRD pattern (Fig. 1a) of CeO_2 exhibited peaks at $2\theta = 28.67°$, 33.09°, 47.49°, 56.41°, 59.11°, 69.71°, 76.73°, 79.21°, and 88.51° corresponding to planes [111], [200], [220] [311], [222], [400], [331], [420], and [422], respectively, of CeO_2 cubic fluorite structure with space group Fm3m (JCPDS: 34-0394) [36, 37]. For ZrO_2, peaks at $2\theta = 24.41°$, 28.31°, 31.61°, and 34.55°, were corresponding to planes [011], [-111], [111], and [200], respectively, of monoclinic zirconia (m-ZrO_2) [JCPDS: 37-1484] [3, 38]. The peaks at $2\theta = 30.37°$, 34.37°, 50.43°, and 60.31° can be assigned to either planes [101], [110], [112], and [211], respectively, of tetragonal zirconia (t-ZrO_2) [JCPDS: 80-0965] or planes [111], [200], [220], and [311] of cubic zirconia (c-ZrO_2) [JCPDS: 27-0997] [36, 38, 39]. The more broadened XRD peaks of $Ce_{0.5}Zr_{0.5}O_2$ observed at $2\theta = 28.93°$, 33.65°, 48.12°, and 57.13° related to the ceria cubic fluorite structure. However, it is reported that the XRD pattern limits the distinction of tetragonal and cubic phases [4, 26]. Further, Raman spectra of the samples confirmed the formation of primarily cubic fluorite crystal structure (Fig. S1), indicating retention of the original crystal structure in $Ce_{0.5}Zr_{0.5}O_2$. The obtained results are in line with previous literature that suggested 2θ varies from 28° to 29°, 33° to 34°, 47° to 48°, and 54° to 57° corresponding to [111], [200], [220], and [311] planes, respectively [4, 36]. Further, a distinguishable peak shifting was observed for the XRD pattern of $Ce_{0.5}Zr_{0.5}O_2$ compared to CeO_2. The peak shifting toward higher 2θ in solid solution is the outcome of the unit cell's shrinkage due to substitution of larger Ce^{4+} ions (~ 0.97 Å) with smaller Zr^{4+} cations (~ 0.84 Å [40, 41]. The formation of a solid solution is critical for the material's thermal stability [40, 41]. The crystallite size obtained from the XRD pattern is as follows: CeO_2-14.74 nm, $Ce_{0.5}Zr_{0.5}O_2$-4.62 nm, and ZrO_2-22.81 nm.

Figure S2 represents the XRD pattern of NiO-loaded CeO_2, ZrO_2, and $Ce_{0.5}Zr_{0.5}O_2$ synthesized by co-precipitation. The XRD patterns revealed peaks of cubic NiO at 2θ = 37·37°, 43·41°, 62·99°, 75.51°, and 79·49° corresponding to planes [111], [200], [220], [311], and [222], respectively [JCPDS: 47–1049] [36]. In the presence of NiO, the XRD peaks corresponding to supports experienced some alteration (Fig. 1a). NiO-CeO_2 exhibited peaks corresponding to cubic phase, similar to pure CeO_2. NiO-ZrO_2 exhibited diffraction peaks related to tetragonal/cubic phases, while pure ZrO_2 exhibited mixed phases.

The peaks for NiO-$Ce_{0.5}Zr_{0.5}O_2$ are broadened compared to $Ce_{0.5}Zr_{0.5}O_2$ because of the strong interaction between NiO and support prepared by co-precipitation [42]. The prepared NiO-containing samples were reduced at 823 K for 2 h using H_2 to obtain metallic Ni-loaded support, and the XRD patterns are represented in Fig. 1b. Three peaks are observed at $2\theta = 44.61°$, 51.97°, and 76.71° confirmed the presence of metallic Ni (JCPDS# 45–1027) [36]. Further, peaks broadening is observed for Ni-$Ce_{0.5}Zr_{0.5}O_2$ due to the transition distortion of the cubic fluorite structure [41, 43]. The peaks broadening also indicates the formation of smaller crystallite [41, 43]. Peak shifting is also observed in the XRD pattern of reduced catalysts, further confirming the solid solution for supported Ni catalyst [1, 36]. The crystallite size of the reduced catalyst obtained from the XRD pattern is as follows: Ni-CeO_2–12.21 nm, Ni-$C_{0.5}Z_{0.5}O_2$–5.77 nm, and Ni-ZrO_2–19.89 nm.

The XPS analysis of the NiO-$Ce_{0.5}Zr_{0.5}O_2$ was performed and represented in Fig. 2. The high-resolution Ni2p XPS profiles appear as broad-spectrum, indicating Ni^{2+} corresponding to a $2p_{3/2}$ peak at

Figure 1 XRD patterns of **a** supports and **b** catalysts (reduced).

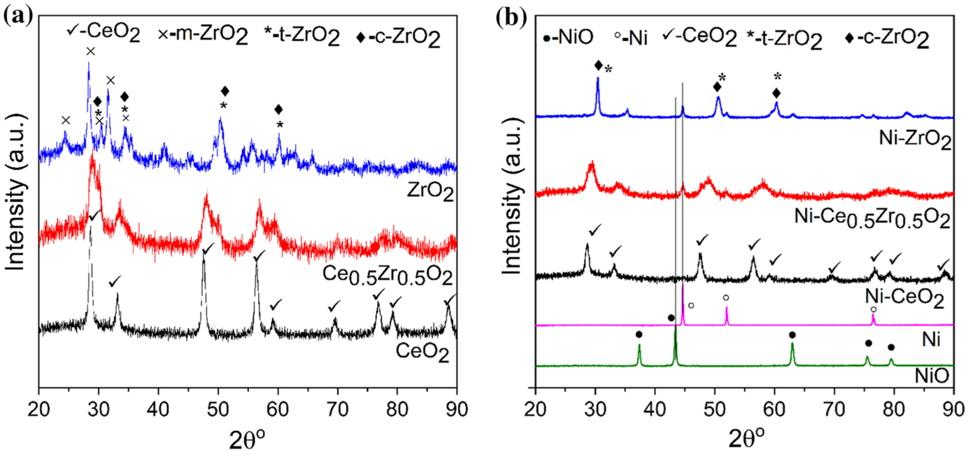

855.2 eV. Ni^{2+} peak position is shifted compared to isolated NiO (~ 853.7 eV) toward higher binding energy due to solid solution formation [10]. Additionally, the higher binding energy of Ni element than pure NiO indicates the formation of strong metal–support interaction [10, 17]. The high-resolution XPS spectra of Ce3d core-level electron (Fig. 2b) reveal a complicated profile consisting of two major sets of spin-orbital multiplets, i.e., $3d_{3/2}$ (u) and $3d_{5/2}$ (v). The complex shape of the Ce3d spectrum was observed because of the interaction of Ce4f and O2p electrons, which are denoted by using the superscript for peak u and v [39]. The assigned peaks v and v'' are a mix of Ce $3d^9$ $4f^2$ $O2p^4$ and Ce $3d^9$ $4f^1$ $O2p^5$ Ce^{4+} final states, while the peak labeled v''' is corresponding to the Ce $3d^9$ $4f^0$ $O2p^6$ Ce^{4+} final state. On the other hand, peaks v^0 and v' are denoted for Ce $3d^9$ $4f^2$ $O2p^5$ and Ce $3d^9$ $4f^1$ $O2p^6$ of Ce^{3+}, respectively.

Figure 2 XPS spectra of **a** Ni2P **b** Ce3d **c** Zr3d and **d** O1s for NiO-$Ce_{0.5}Zr_{0.5}O_2$.

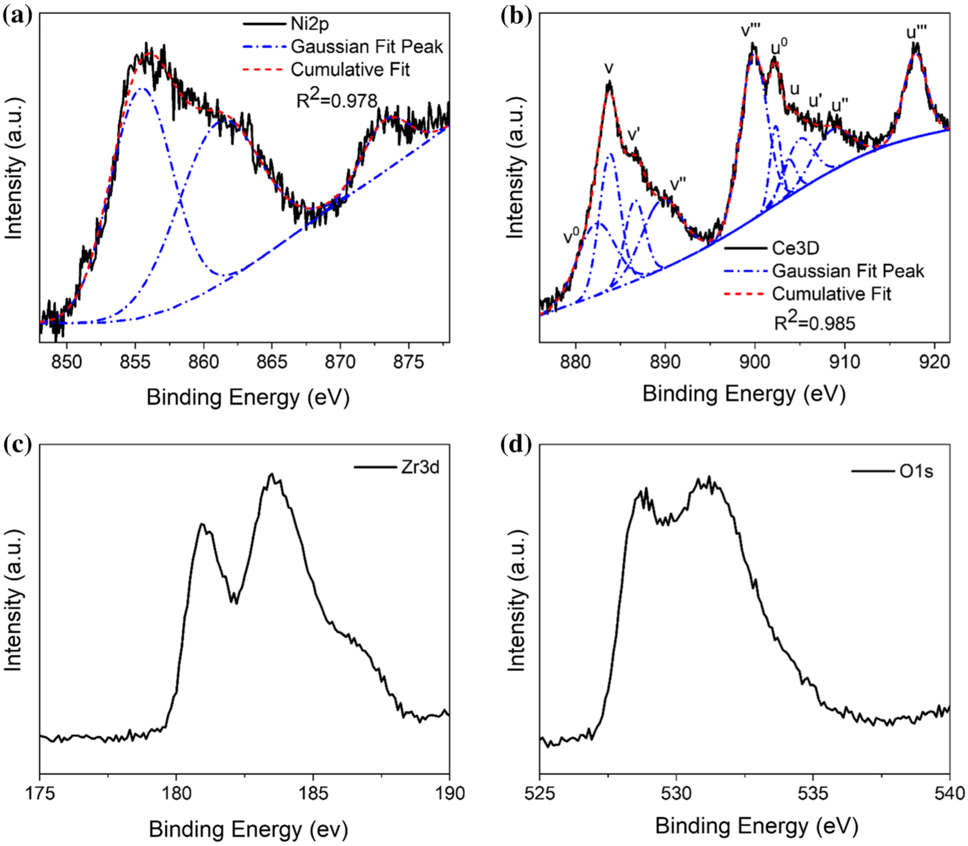

Similarly, *u* structures are assigned to correspond to the Ce $3d_{3/2}$ levels. The present spectra suggest the presence of both Ce^{3+} and Ce^{4+} [8, 10, 39]. The % Ce^{3+} was calculated according to the following equation [44, 45]:

$$[Ce^{3+}]\% = \frac{A_{v^0} + A_{v'} + A_{u^0} + A_{u'}}{A_v + A_{v''} + A_{v'''} + A_u + A_{u''} + A_{u'''}} \times 100 \tag{1}$$

where A_i is the area of the corresponding peaks.

The $\%Ce^{3+}$ was calculated to be ~ 47 for NiO-$Ce_{0.5}Zr_{0.5}O_2$. Additionally, the $\%Ce^{3+}$ was also estimated for NiO-CeO_2 as shown in Fig. S3 and found to be ~ 25. The increase of % Ce^{3+} denotes the improvement of oxygen vacancy for NiO-$Ce_{0.5}Zr_{0.5}O_2$ catalyst. Further, the Zr3d spectrum shows two peaks at 180.8 ($3d_{5/2}$) and 183.4 ($3d_{3/2}$) eV corresponding to Zr^{4+} confirm the presence of Zr in the CeO_2 cubic fluorite structure [10]. The O1s XPS profile also indicated multiple oxygen species corresponding to the prepared solid solution. Two major peaks at 528.6 and 531.1 eV correspond to lattice oxygen and oxygen vacancies due to the presence of a large amount of Ce^{3+} [8, 10]. It is noted that there are no peaks found corresponding to the Na species as NaOH was used as precipitating agent, confirming the precipitate was appropriately washed to remove impurities.

The HRTEM images of NiO-$Ce_{0.5}Zr_{0.5}O_2$ were also acquired. The low magnified image (Fig. 3a) displays the distribution of small NiO nanoparticles over the $Ce_{0.5}Zr_{0.5}O_2$ support. The particle size distribution reveals most NiO nanoparticles are in the size range of ~ 12 to 15 nm (inset Fig. 3a). The high-resolution image displays a highly crystalline structure of the solid solution. The lattice *d*-spacing of 0.32 nm corresponding to (111) plane of fluorite cubic structure of ceria confirms solid-solution formation [44]. The *d*-spacing of 0.24 nm also ensures the (111) plane of NiO [46]. The images also unveil the strong interaction between NiO and support, as observed in XPS and XRD analysis. Fig. S4 represents a high-resolution SEM image and elemental mapping analysis. The HRSEM image (Fig. S4a) displays the small NiO nanoparticles on larger support nanoparticles and also confirms the distribution of NiO nanoparticles. The elemental mapping analysis (Fig. S4 b–f) confirms homogeneous dispersion of Ni, Ce, Zr, and O, further supporting the solid solution formation.

Oxygen storage capacity and temperature-programmed reduction

The OSC was assessed by the O_2 pulse injection method for CeO_2, ZrO_2, and $Ce_{0.5}Zr_{0.5}O_2$, and the results are presented in Fig. 4a and S5. Here, it should be noted that measurement of OSC at DRM reaction temperature by oxygen pulse injection technique is rare. It can be observed from Fig. 4a that the OSC of pure CeO_2 and ZrO_2 is ~ 14.3 and 3.5 mol/g, whereas, for $Ce_{0.5}Zr_{0.5}O_2$, it increases to 16.9 mol/g. The high OSC is attributed to the enhanced ratio of Ce^{3+}/ Ce^{4+} and oxygen vacancy due to the presence of Zr^{4+}, as also observed in XPS analysis [2, 3, 10, 43, 47].

The H_2-TPR profiles for the supported NiO catalysts were recorded and represented in Fig. 4b. The reduction temperature of pure NiO was ~ 697 K. For NiO-CeO_2, two reduction peaks are observed at a reduction temperature of ~ 535 and ~ 613 K. The former peak appeared due to surface reduction, while the later peak was for bulk reduction. For NiO-ZrO_2, two reduction peaks are observed around 662 and 790 K. For NiO-$Ce_{0.5}Zr_{0.5}O_2$, the single reduction peak is observed ~ 663 K. Relatively low-temperature reduction peak corresponding to NiO-CeO_2 was observed due to the increased reducibility of the metal oxide loaded on ceria [9, 38]. In NiO-ZrO_2, the peak-shifting toward higher reduction temperature can be ascribed to the presence of stable oxide species, which is hard to reduce [17, 48]. The single reduction peak at a higher temperature for NiO-$Ce_{0.5}Zr_{0.5}O_2$ can be attributed to the stronger interaction of the metal with the solid solution and the presence of mobile oxygen as established from XPS and HRTEM analysis [6, 47]. Further, the reason behind the single peak for NiO-$Ce_{0.5}Zr_{0.5}O_2$ catalyst is that as soon as the surface oxygen is being reduced, the bulk oxygen comes to the surface due to the increased mobility or chemical diffusion of oxygen; as a result, continuous reduction of metal oxide is observed [49, 50]. The incorporated Zr^{4+} increases oxygen vacancies, enhances the bulk oxygen diffusion/mobility, and helps to improve the OSC and redox properties [15, 51]. Additionally, the widening of the reduction peak implied wide particle size distribution and stronger interaction with support at a higher temperature compared to purely supported catalysts [3, 52].

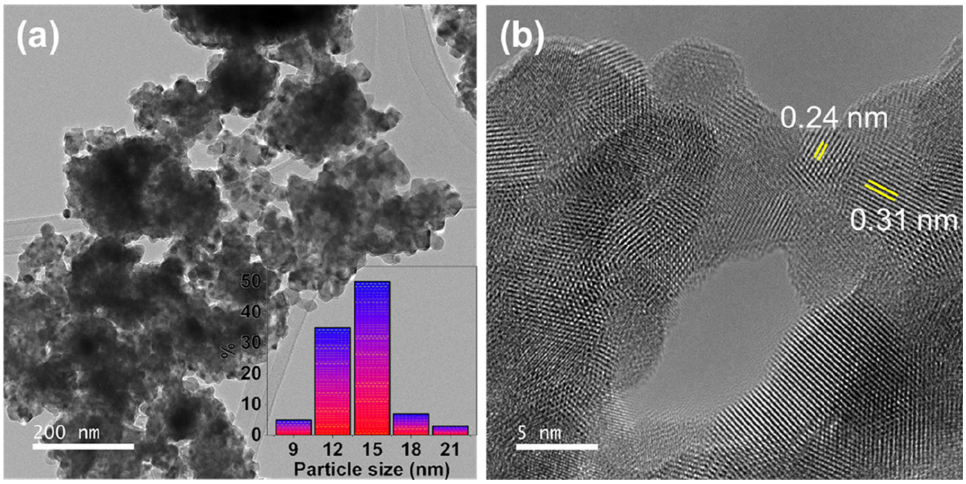

Figure 3 **a**, **b** HRTEM images of NiO-$Ce_{0.5}Zr_{0.5}O_2$. The particle size distribution of NiO in inset *a*.

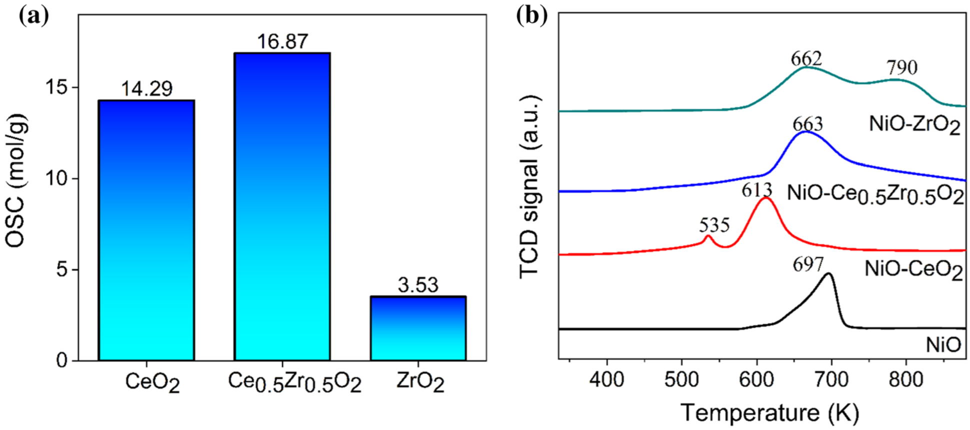

Figure 4 The profiles of **a** OSC for supports **b** H_2-TPR for calcined catalysts.

Temperature-programmed desorption

The H_2-TPD profiles were obtained from 323 to 800 K and are shown in Fig. 5a. Two H_2 desorption peaks (after deconvolution) are observed, which indicate two types of surface-active metal sites. The higher temperature peak denotes strongly bonded hydrogen species [5, 7]. The peaks for Ni-CeO_2 are at ~ 510 and 640 K, while the peaks for Ni-ZrO_2 are observed at comparatively lower temperatures at ~ 430 and 560 K. Further lower temperature peaks (~ 395 and 500 K) are identified for Ni-$Ce_{0.5}Zr_{0.5}O_2$. The desorption peaks for Ni-$Ce_{0.5}Zr_{0.5}O_2$ are broader than Ni-CeO_2 and Ni-ZrO_2, which can be ascribed to an increment of surface-active metal sites due to incorporation of Zr^{4+} into ceria as the peak area is increased [7]. The calculated amount of surface-active metal sites for the catalysts is tabulated in Table 1. It can be observed that the amount of surface-active metal sites is 67 and 31 μmol/g for Ni-CeO_2 and Ni-ZrO_2, respectively. The highest amount of surface-active metal sites is obtained for Ni-$Ce_{0.5}Zr_{0.5}O_2$ (75 μmol/g). Hence, it can be realized that the Ni-$Ce_{0.5}Zr_{0.5}O_2$ exhibited the best metal dispersion, which might be extrapolated from the results obtained from XRD, HRTEM, and H_2-TPR analysis.

The basic sites available on the surface of the catalysts were characterized by CO_2-TPD, and the profiles are shown in Fig. 5b. It is assumed that the quantity of CO_2 consumed is equal to CO_2 desorbed and is the measurement of the basicity of the catalyst [7]. The amount of CO_2 desorbed for the catalysts is tabulated in Table 1. The CO_2 desorption profiles deconvoluted to multiple peaks in the temperature range of 323–800 K suggest desorption of CO_2 is a function of temperature, indicating the basic sites of different strengths [53]. The peaks at low temperature and high temperature are attributed to the desorption of CO_2 from support and metal, respectively [54]. The low-temperature peak (~ 405–440 K) is gradually shifted toward a higher temperature in the order of Ni-CeO_2 < Ni-$C_{0.5}Z_{0.5}O_2$ < Ni-ZrO_2. Further, the

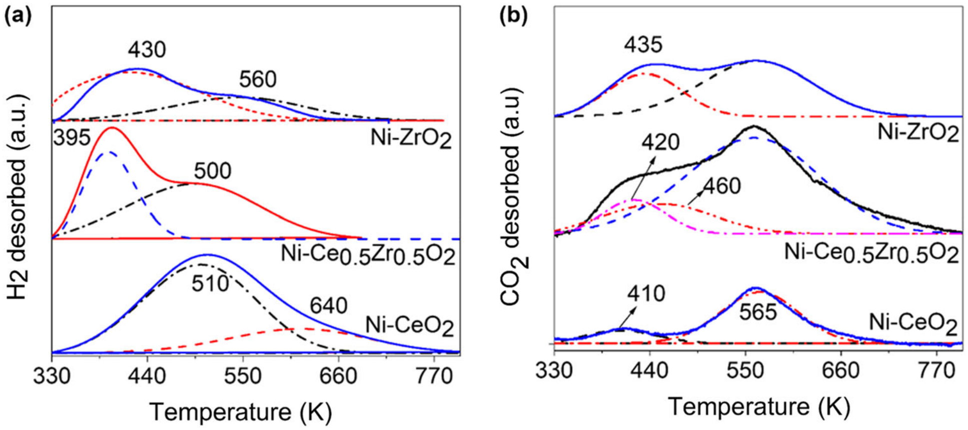

Figure 5 The profiles of **a** H_2-TPD **b** CO_2-TPD for reduced catalysts.

Table 1 Characterizations information of H_2-TPD and CO_2-TPD for reduced catalysts

Catalysts	H_2 desorbed (μmol/g) from H_2-TPD analysis	CO_2 desorption (μmol/g) from CO_2-TPD analysis
Ni-CeO_2	67	40
Ni-$Ce_{0.5}Zr_{0.5}O_2$	75	94
Ni-ZrO_2	31	88

peaks' shape suggests an increment of desorbed CO_2 can be correlated to the amount of surface-active metal sites observed in H_2-TPD (Table 1). The higher temperature peak (~ 565 K) displayed maximum CO_2 desorption for Ni-$C_{0.5}Z_{0.5}O_2$ (Table 1) credited to solid solution formation. The adsorption and activation of CO_2 are facilitated by enriched oxygen vacancies as well as improved basic sites (Table 1) [53, 54].

Oxygen vacancy formation energies (OVFE): effect of Zr substitution

The model structures of CeO_2, $Ce_{0.5}Zr_{0.5}O_2$, and ZrO_2 are shown in Fig. 6, and the geometry-optimized structural parameters of the three systems are reported in Table 2. It is evident that the substitution of 50% atomic Ce by the same amount of Zr resulting in $Ce_{0.5}Zr_{0.5}O_2$ structure produced large perturbation in cell parameters. The decrease in the mixed oxide cell parameter from pure ceria is due to the substitution of smaller Zr^{4+} cations (~ 0.84 Å) into larger Ce^{4+} ions (~ 0.97 Å), confirming the formation of mixed solid solution. These findings are in line with the other reported results [19, 25]. Importantly, perturbation in cell parameters was more for the mixed oxide structure compared to their oxide counterpart. Additionally, the nearest O anions move toward the vacancy site, while cations (Ce^{3+} and Zr^{4+}) move away from it in the defect structure. As a result of such displacement and structural distortion, the redox properties of the oxides are affected [19, 25]. This distortion led to having shorter (2.344–2.345 Å) Ce–O and longer (2.248 Å) Zr-O interatomic distances when compared with the pure oxide (2.373 for Ce–O in CeO_2 and 2.218 for Zr-O in ZrO_2) structures. The decrease in Ce–O distance caused by Zr addition was also observed in EXAFS and XANES measurements [19]. These interatomic distances are reported in Table S1 (in supplementary section), and it is clear that the extent of distortion was more for all the defect structures than their original ones. Such a large

Table 2 Geometric parameter and oxygen vacancy formation energy of CeO_2, $Ce_{0.5}Zr_{0.5}O_2$, and ZrO_2

Model	Optimized lattice parameter (Å)		Oxygen vacancy formation energy (eV)
	original	defect	
CeO_2	$a = b = c = 10.962$	$a = 10.975$, $b = 10.976$, $c = 10.977$	3.70
$Ce_{0.5}Zr_{0.5}O_2$	$a = b = 10.619$, $c = 10.566$	$a = 10.641$, $b = 10.642$ $c = 10.572$	3.20
ZrO_2	$a = b = c = 10.243$	$a = b = 10.242$, $c = 10.243$	5.95

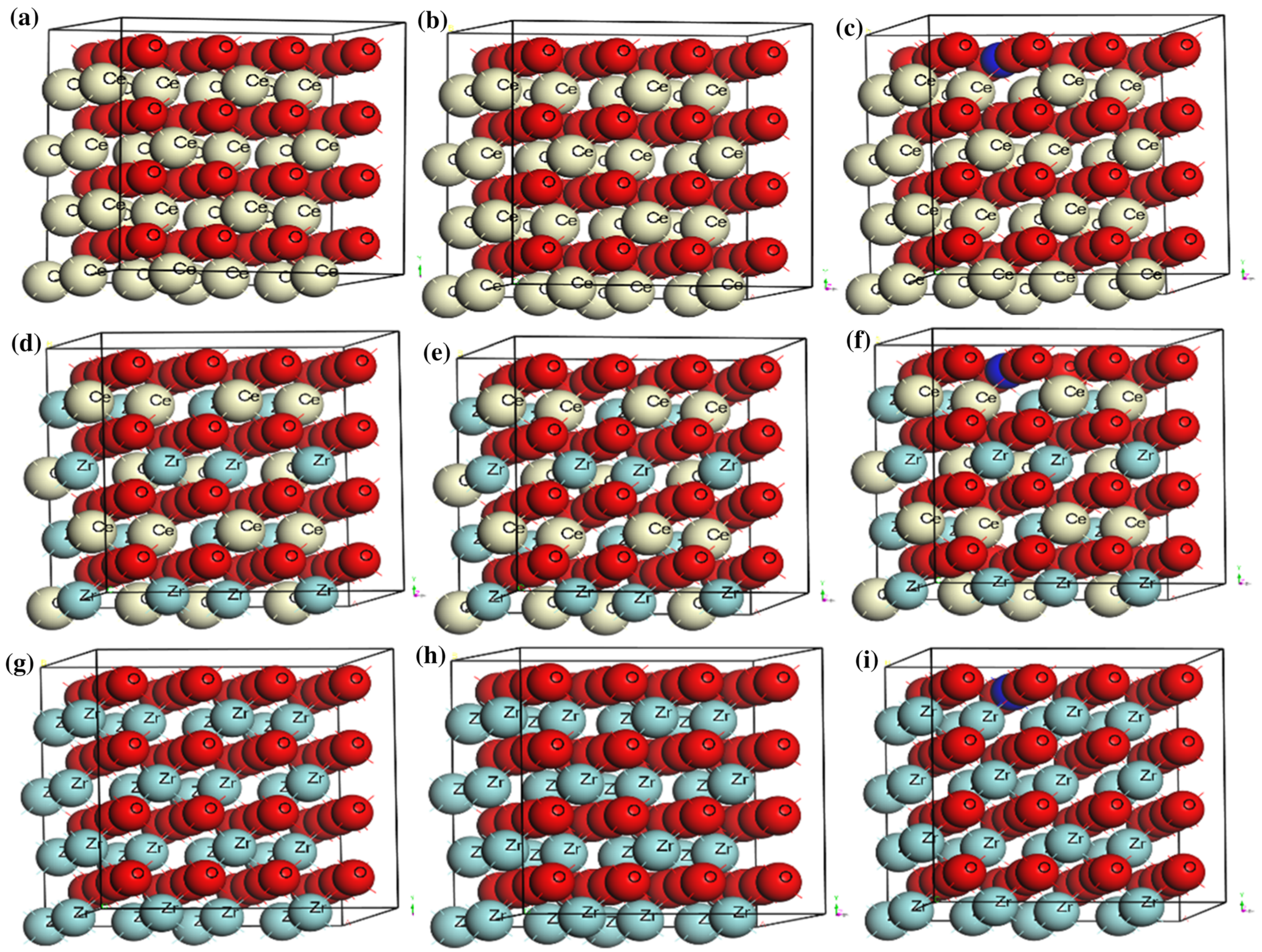

Figure 6 Model structure for (2 × 2 × 2) supercell of **a** pristine CeO_2 **b** CeO_2 optimized **c** defect CeO_2 optimized **d** $Ce_{0.5}Zr_{0.5}O_2$ **e** $Ce_{0.5}Zr_{0.5}O_2$ optimized **f** defect $Ce_{0.5}Zr_{0.5}O_2$ optimized **g** ZrO_2 **h** ZrO_2 optimized **i** defect ZrO_2 optimized. The blue color represents the vacant position (V = 0.375, 0.625, 0.625) of one oxygen atom vacancy. Atoms presented in red, light yellow, and light blue color are for oxygen, ceria, and zirconia, respectively.

range of cation–oxygen interatomic distances in the defect structures have effects on OVFE.

The oxygen vacancy formation energy obtained after DFT calculation for CeO_2 was 3.70 eV, which is in good agreement with the reported theoretical value of 3.72 [19]. The highest value of E_v^f was calculated nearby 5.95 eV for ZrO_2, which is slight higher value compared to 5.89 and 5.86 eV reported previously [18, 19]. This difference may be due to the full relaxation of the cell and the convergence tolerance used in our calculations. When 50% cerium is substituted by 50% zirconium in $Ce_{0.5}Zr_{0.5}O_2$, the E_v^f was decreased to 3.20 eV. As reported in Table 2, the introduction of Zr in ceria lowered the E_v^f of ceria ~ 0.50 eV [19]. The lowering in E_v^f of $Ce_{0.5}Zr_{0.5}O_2$ structure is consistent with previous studies which confirmed that it is easier to create oxygen vacancy for Zr-substituted CeO_2 ($Ce_{0.5}Zr_{0.5}O_2$) than pure CeO_2 [18]. Such a reduction in the oxygen vacancy formation energy also suggests that the Zr-doping can serve as nucleation centers for vacancy clustering [25, 55].

The decrement of lattice parameters by the addition of Zr^{4+} suggested the formation of solid solution, as revealed by our experimental XRD results. The solid solution formed was of the type $Ce_xZr_{1-x}O_2$ and possessed a smaller crystallite size. The reduction of E_v^f value suggests that the reducibility of $Ce_{0.5}Zr_{0.5}O_2$ is greatly enhanced by the incorporation of Zr^{4+} into ceria to form mixed solid solution $Ce_xZr_{1-x}O_2$ [25]. Additionally, the incorporation of Zr^{4+} into ceria lowers the E_v^f for $Ce_{0.5}Zr_{0.5}O_2$, and the lowest value of E_v^f compared to pure ceria and zirconia attributing increased reducibility and the highest OSC [18, 19, 25]. These results are in accordance with our experimental OSC, H_2-TPR, and XPS observations.

Previous studies have attempted to rationalize the origin of OVFE by correlating with structural relaxation energy (E_{relax}), displacements of O anion near the oxygen vacancy site, ionic radius of metal dopant, phases of crystal, and localization f electron in the presence of oxygen vacancies [18–20, 25]. In addition to this, Lin et al. established a relationship between the structural properties and chemical reactivity of doped ceria experimentally by correlating OSC with oxygen vacancy concentration, degree of crystallinity, and lattice dimensions [56]. Very recently, Hinuma et al. proposed that band gap (BG), bulk formation energy (BFE), electron affinity (EA), ionization potential (IP), and surface energy (SE) strongly influence surface OVFE [57]. Based on these previous results, it seemed that bulk or surface OVFE is caused due to bulk lattice structure and its physicochemical nature, such as oxygen vacancy concentration, oxygen storage capacity. It would be worthwhile to obtain a descriptor by developing a structure-activity or structure-property relationship. The development of descriptors is crucial for understanding catalytic phenomena and designing new and better materials. In the present study, we have correlated the experimentally observed catalytic property, i.e., oxygen storage capacity (OSC), and computationally calculated structural property, i.e., oxygen vacancy formation energy (OVFE). The R^2 value (0.999) of the fitted line revealed linearity between OSC and OVFE, as shown in Fig. 7. Interestingly, this fitted line indicates that lower the OVFE, higher OSC will be obtained as vacancies can be created easily. Thus, OVFE can be used as a descriptor of materials functionality, such as the oxygen storage capacity of the supports.

Catalytic activity

The improved OSC, surface-active metallic dispersion, and basicity of prepared Ni-$C_{0.5}Z_{0.5}O_2$ were validated for the DRM reaction at 873 K for 4 h. The percentage conversions of CH_4, CO_2, and the ratio of H_2/CO were calculated and are shown in Fig. 8. It may be noted that a catalyst could not be thoroughly examined and compared at equilibrium conversions. Hence, the operating criteria ensured plug flow conditions during the reactions, minimizing back mixing, channeling, and avoiding heat and mass transfer limitations, resulting in low conversion than the equilibrium conversion [7, 58]. It can be observed from Fig. 8a, b, the highest conversions of CH_4 and CO_2 are ∼ 8.7% and ∼ 12.4% for Ni-$C_{0.5}Z_{0.5}O_2$, far away from the chemical equilibrium conversions at the same operating conditions previously reported around 53% and 63% for CH_4 and CO_2, respectively [59]. The conversion of CH_4 for Ni-$C_{0.5}Z_{0.5}O_2$ is ∼ 2.4 and 3 times higher than Ni-CeO_2 and Ni-ZrO_2, respectively. Similarly, the conversion of CO_2 for Ni-$C_{0.5}Z_{0.5}O_2$ is also observed higher than Ni-CeO_2 and Ni-ZrO_2 and, i.e., ∼ 1.4 and 1.7 times, respectively.

Moreover, the conversion of CO_2 is higher than that of CH_4 for all the catalysts. It might be attributed to the following possible reasons: (i) the reverse water gas shift reaction ($H_2 + CO_2 \leftrightarrow H_2O + CO$), resulting in more CO_2 consumption; (ii) more CO_2 adsorption on the surface of support due to its basicity, reducing the surface to replenish the consumed oxygen from its lattice; and (iii) the reaction of activated CO_2 and CH_x (i.e., surface adsorbed CH_4) to produce CO and H_2 [7, 60]. Simultaneously, more CO is converted via CO disproportionation ($2CO \leftrightarrow C + CO_2$) and CO hydrogenation ($CO + H_2 \leftrightarrow C + H_2O$), respectively. Thus, it influences syngas production and leads to the H_2/CO ratio less than unity for all catalysts [6, 31, 43].

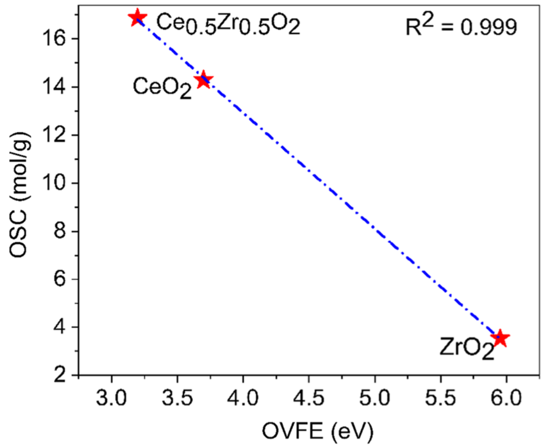

Figure 7 Correlation between oxygen vacancy formation energy and oxygen storage capacity of CeO_2, $Ce_{0.5}Zr_{0.5}O_2$, and ZrO_2 supports.

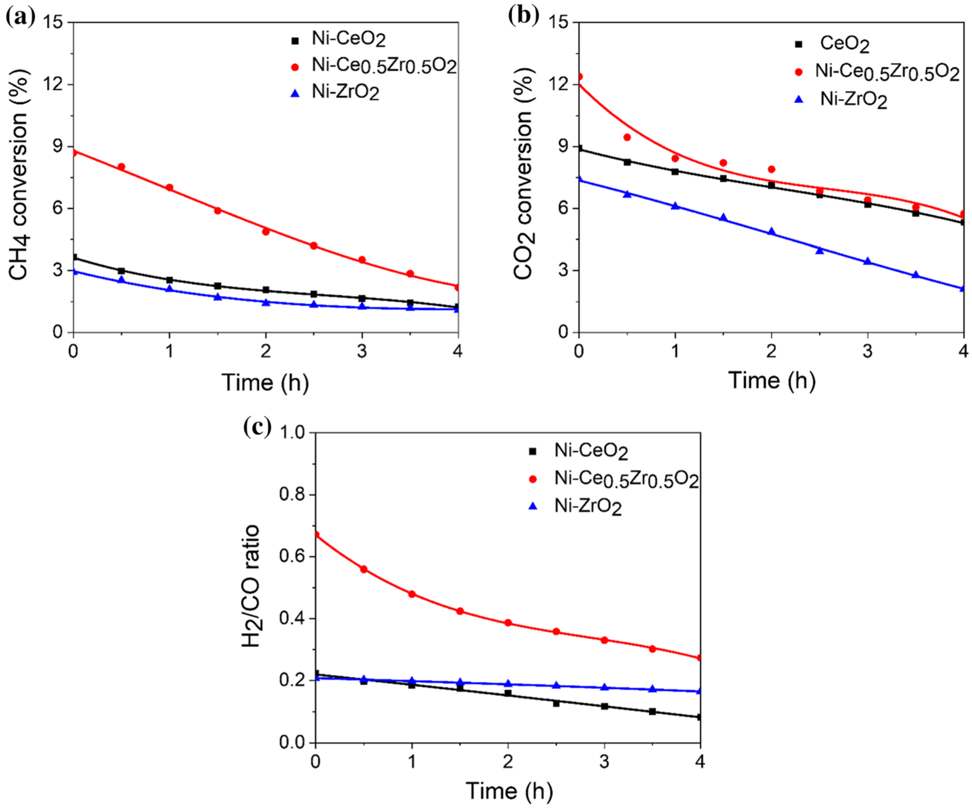

Figure 8 Catalytic activities test of catalysts for DRM reaction **a** % CH_4 conversion **b** % CO_2 conversion **c** H_2/CO ratio. Reaction conditions: $CH_4/CO2/N_2 = 1:1:3$ (volumetric flow rate), $W/F_{A0,CH_4} = 1.19$ $kg_{cat.}h\ (kmol\ of\ CH_4)^{-1}$; GHSV = 60,000 ml g^{-1} h^{-1} and reaction temperature = 873 K at atmospheric pressure. At 873 K, the equilibrium conversion of CH_4, $CO_{2,}$ and H_2/CO was obtained around 52.67%, 63.60%, and 0.81, respectively [59].

From Fig. 8a, b a gradual decrease in the conversions of CH_4 and CO_2 can be observed with TOS (time on stream). The conversion of CO_2 for Ni-$C_{0.5}Z_{0.5}O_2$ reduced quickly for 1 h of TOS and then became sluggish for the next 1 h. The conversion for Ni-ZrO_2 decreased rapidly, whereas the conversion for Ni-CeO_2 changed gradually throughout the TOS. After 4 h of TOS, the conversions for all materials were reduced to less than half of the initial value. However, Ni-$C_{0.5}Z_{0.5}O_2$ exhibited better performance than Ni-CeO_2 and Ni-ZrO_2. A wide range of conversions were reported for different reaction conditions. The conversions are varied due to catalyst synthesis processes, loading of active metals, supporting materials, reactor design, and operating conditions. For example, Makri et al. observed the conversions of CH_4 and CO_2 ~ 14.5% and 16.5%, respectively, at 873 K with GHSV = 30,000 h^{-1} for 5 wt. % Ni-$Ce_{0.5}Zr_{0.5}O_2$ and realized that it is a function of Ce/Zr ratio and temperature [61], whereas Xu et al. reported the conversions of CH_4 and CO_2 are ~ 49.43% and 56.71% at 1023 K, GHSV = 60,600 ml g^{-1} h^{-1} for 7 wt.% Ni/$Ce_{0.5}Zr_{0.5}O_2$ [10].

The H_2/CO ratio is considered a critical parameter for the activity comparison of the DRM catalysts. The H_2/CO is calculated from reaction data and is shown in Fig. 8c. It can be observed that the H_2/CO ratio for all the catalysts was less than unity, confirming the occurrence of side reactions as discussed earlier. The highest value for H_2/CO ratio is ~ 0.67 for Ni-$C_{0.5}Z_{0.5}O_2$, while the equilibrium H_2/CO ratio is 0.73 at the studied reaction conditions as reported by García-Diéguez et al. [59]. The H_2/CO ratio for Ni-$C_{0.5}Z_{0.5}O_2$ is observed to be ~ 3 times more than Ni-CeO_2 and Ni-ZrO_2; however, it decreased with TOS. The initial H_2/CO ratio is similar for Ni-CeO_2 and Ni-$ZrO_{2;}$ however, the H_2/CO ratio for Ni-CeO_2 decreased gradually and became the least after 4 h of TOS. In line with our findings, previous studies also reported the highest H_2/CO ratio for Ni-$C_{0.5}Z_{0.5}O_2$ at different operating conditions [6, 17, 62, 63]. L. Xu reported the H_2/CO ratio is ~ 0.64 over 7wt. % Ni/$C_{0.5}Z_{0.5}O_2$ at 1023 K, GHSV = 60,600 ml g^{-1} h^{-1} [10]. M.M. Makri et al. reported H_2/CO ratio is ~ 0.36 at 873 K with GHSV = 30,000 h^{-1} for 5wt. % Ni/$Ce_{0.5}Zr_{0.5}O_2$ and showed that it is temperature-dependent [61].

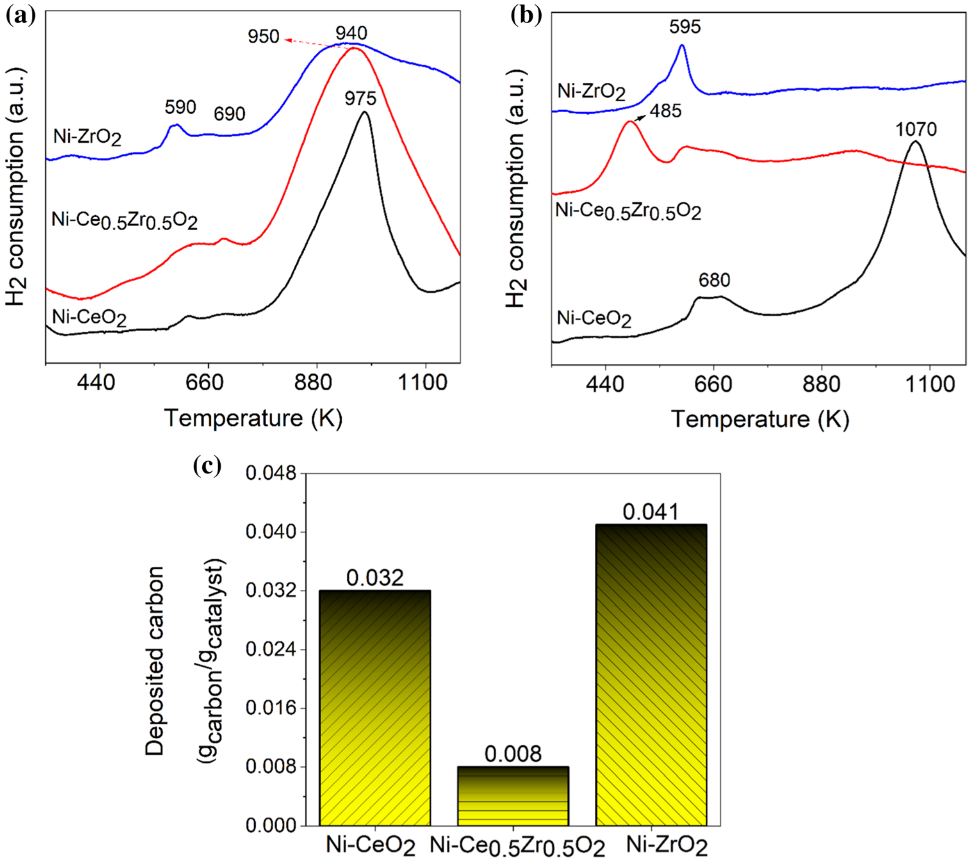

Figure 9 TPH profiles of **a** CH4 cracking, **b**DRM reaction for reduced catalysts, and **c** deposited carbon on catalysts during catalytic activities test.

The turnover frequency for $Ni-C_{0.5}Z_{0.5}O_2$ was calculated based on CH_4 conversion for DRM reaction (TOF_{DRM}) using surface-active metal sites from H_2-TPD data. The initial value of TOF_{DRM} for $Ni-C_{0.5}Z_{0.5}O_2$ is ~ 0.27 s^{-1}, and it decreased to 0.13 s^{-1} at the 4th hour. The TOF of a catalyst also depends on the reaction parameters, e.g., TOF_{DRM} was observed ~ 0.081 s^{-1} for 5wt.% Ni/ $Ce_{0.5}Zr_{0.5}O_2$ at 823 K, GHSV = 30000 h^{-1} [61]; ~ 1.8 s^{-1} for 5 wt.% Ni/ $Ce_{0.6}Zr_{0.4}O_2$ at 873 K, at GHSV = 60,000 ml g^{-1} h^{-1} [43]; ~ 8.3 s^{-1} for 15 wt.% Ni/ $Ce_{0.5}Zr_{0.5}O_2$, at 1073 K; GHSV = 216,000 ml g^{-1} h^{-1} [42]. The enhancement in conversions and H_2/CO ratio for $Ni-C_{0.5}Z_{0.5}O_2$ is observed due to improved OSC, metal reduction, higher surface-active metal sites, and different types of basicity.

Carbon characterization and analysis

CH_4 cracking is a crucial step during the DRM reaction and an imperative source of carbon deposition along with other side reactions [31]. To investigate types of carbon formed along with their sources during DRM, a TPH study was performed after cracking of CH_4, CO_2, and r-DRM reaction, respectively, for 0.17 h at 873 K over each catalyst, and the profiles are shown in Fig. 9a, b. It is assumed that under similar DRM reaction conditions, the CH_4 will be cracked to give various carbonaceous species like CH_x (x = 0–3), which will be hydrogenated during the experiment, and the formed carbonaceous species will be characterized by obtained TPH profiles [29, 31]. It should be noted that the other reactant of DRM, i.e., CO_2, was not cracked under similar experimental conditions to give any detectable carbonaceous species by TPH [5]. Based on TPH, carbonaceous species are classified as: α, β, and γ [48]. The reactivity of carbonaceous species is in the order of $\alpha > \beta > \gamma$, which indicated γ is the most challenging carbonaceous species to be hydrogenated. Multiple TPH peaks are observed (Fig. 9a) at different temperature ranges after CH_4 cracking. Low-temperature weak TPH peaks in the range of 590–690 K are observed for all the catalysts indicating α-carbon. An intense TPH peak in the temperature range of 940–975 K is observed for all the catalysts indicating

Table 3 Carbon characterization and analysis

Catalysts	H_2 consumed (μmol/g) from TPH analysis	
	CH_4 cracking	DRM reaction
Ni-CeO_2	1594	950
Ni-$Ce_{0.5}Zr_{0.5}O_2$	1869	210
Ni-ZrO_2	1043	410

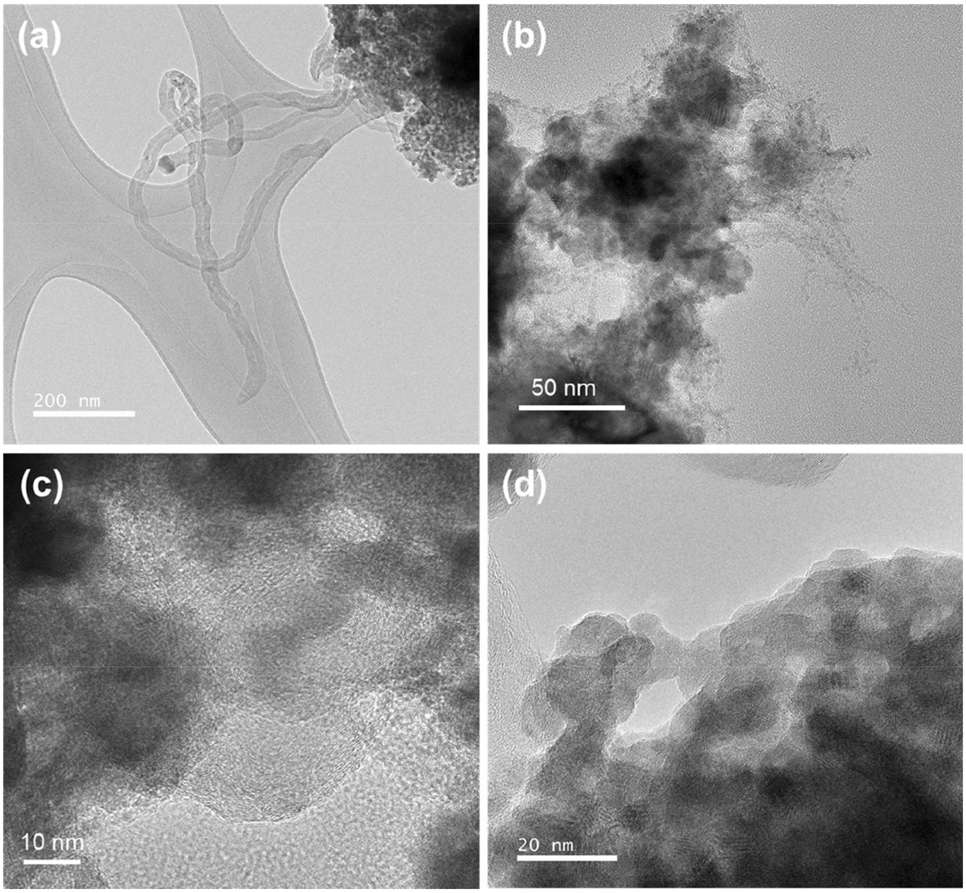

Figure 10 **a**–**d** HRTEM images of spent catalyst (Ni-$Ce_{0.5}Zr_{0.5}O_2$).

β-carbon. Typically, low-temperature TPH peaks were observed for all the catalysts after *r*-DRM reaction (Fig. 9b), in the temperature range of 485–680 K, indicating the presence of α-carbon. However, the Ni-CeO_2 revealed an intense TPH peak at ~ 1070 K, indicating the presence of *γ*-carbon; a hump for Ni-$C_{0.5}Z_{0.5}O_2$ can be observed at ~ 940 K, denoting the deposition of *β*-carbon.

A comparison of Fig. 9a, b suggests that the most reactive α-carbon is present on all the spent catalysts after *r*-DRM. The *β*-carbon is rarely observed as CO_2 might have gasified them [5]; however, *γ*-carbon is observed only for Ni-CeO_2.

The amount of H_2 consumed during TPH experiments is tabulated in Table 3. The uptake of H_2 after CH_4 cracking is maximum for Ni-$C_{0.5}Z_{0.5}O_2$, which indicates that more carbonaceous species are formed as it is the most active catalyst, as discussed (Fig. 8). Interestingly, for r-DRM, the lowest H_2 was consumed by the Ni-$C_{0.5}Z_{0.5}O_2$ suggesting the minimum carbonaceous species deposition, which might be credited to the high OSC and basicity. It predicts the possibility of minimum carbon deposition under DRM reaction. Catalytic materials with high OSC tend to provide oxygen from their lattice; hence the possibility of removing formed carbon via gasification by surface oxygen during the DRM is increased [42, 47]. Simultaneously, the higher basicity of catalytic materials ensures maximum CO_2 adsorption on its surface, converting the deposited carbonaceous species into CO [53, 54]. The CHNSO analyzer was also used to measure the deposited carbon over the catalysts after 4 h of DRM reaction and presented in Fig. 9c. As predicted from the TPH study, minimum carbon deposition is observed over the spent Ni-$C_{0.5}Z_{0.5}O_2$. The OSC of $C_{0.5}Z_{0.5}O_2$ and basicity of Ni-$C_{0.5}Z_{0.5}O_2$ activate the process for the effective redox cycle that facilitates the gasification of deposited carbonaceous species on the active metal surface, thus preventing the deactivation of catalysts [39, 53, 62, 64].

Besides the higher OSC and basicity for Ni-$C_{0.5}Z_{0.5}O_2$, a smaller crystallite size could be one of the reasons for the inhibition of carbon deposition, leading to its higher performance [17, 42, 58]. The carbon formation is also observed in the HRTEM images of the spent Ni-$C_{0.5}Z_{0.5}O_2$ catalyst (Fig. 10). The HRTEM images reveal the formation of carbon nanotube and layers of carbon over the catalyst surface. The formed carbon was also characterized by EDSA, HRTEM-STEM mapping analysis (Fig. S6), revealing uniform dispersion of the carbon. However, interestingly, the catalyst's crystal structure does not show any significant alteration (Fig. 10d).

Conclusion

Ceria-zirconia supports and supported 15 wt.% Ni catalysts were prepared by the one-step co-precipitation method to study the impact of OSC and surface basicity on the catalytic activity. The catalysts were well characterized by various techniques, and the performance was investigated for the DRM reaction. The reducibility of NiO is increased for pure ceria support. Further addition of Zr^{4+} improved the interaction of the metal with the support surface and increased the mobility of oxygen from bulk to the surface. Additionally, incorporation of Zr^{4+} into the ceria-cubic fluorite structure improved the OSC, surface-active metal sites, and basicity. The smaller crystallite size of support and particle size of metallic species confirmed uniform metal dispersion. The highest catalytic activity was obtained for the solid solution-supported catalyst (Ni-$Ce_{0.5}Zr_{0.5}O_2$). The H_2/CO ratio was found to be less than unity suggesting the occurrence of side reactions. The detailed analysis (via TPH) revealed that CH_4 cracking is a significant carbon-forming reaction. The carbon analysis indicated that the catalyst deactivation is limited for the Ni-$Ce_{0.5}Zr_{0.5}O_2$ than that of Ni-CeO_2 and Ni-ZrO_2 due to the higher OSC and basicity, preventing carbon deposition. The improvement in OSC was correlated to E_v^f as revealed from DFT study. A linear correlation was drawn between oxygen storage capacity (OSC) and oxygen vacancy formation energy (OVFE) to propose the latter as a descriptor. Thus, enhanced catalytic activity and low carbon deposition were observed for the ceria-zirconia solid solution-supported Ni catalyst. However, catalyst deactivation and carbon deposition were observed throughout the reactivity test, which may be further addressed by adding suitable basic oxide materials.

Acknowledgements

We acknowledge Central Research Facilities (CRF), IIT (ISM), Dhanbad, India, for different characterizations. A. S. acknowledges the DST-INSPIRE Faculty scheme for Fellowship (Grant No. IFA17-MS107).

Declarations

Conflicts of interest The author declare that they have no conflict of interest.

Supplementary Information: The online version contains supplementary material available at https://doi.org/10.1007/s10853-021-06720-5.

References

[1] Sukonket T, Khan A, Saha B et al (2011) Influence of the catalyst preparation method, surfactant amount, and steam on CO_2 reforming of CH_4 over 5Ni/$Ce_{0.6}Zr_{0.4}O_2$ Catalysts. Energy Fuels 25:864–877. https://doi.org/10.1021/ef101479y

[2] Li P, Chen X, Li Y, Schwank JW (2019) A review on oxygen storage capacity of CeO_2-based materials: influence factors, measurement techniques, and applications in reactions

related to catalytic automotive emissions control. Catal Today 327:90–115. https://doi.org/10.1016/j.cattod.2018.05.059

[3] Kambolis A, Matralis H, Trovarelli A, Papadopoulou C (2010) Ni/CeO_2-ZrO_2 catalysts for the dry reforming of methane. Appl Catal A, Gen 377:16–26. https://doi.org/10.1016/j.apcata.2010.01.013

[4] Devaiah D, Reddy LH, Park S-E, Reddy BM (2018) Ceria–zirconia mixed oxides: synthetic methods and applications. Catal Rev 60:177–277. https://doi.org/10.1080/01614940.2017.1415058

[5] Kumari R, Sengupta S (2020) Catalytic CO_2 reforming of CH_4 over $MgAl_2O_4$ supported Ni-Co catalysts for the syngas production. Int J Hydrog Energy 45:22775–22787. https://doi.org/10.1016/j.ijhydene.2020.06.150

[6] Zhang F, Liu Z, Chen X et al (2020) The Effects of Zr-doping into ceria for the dry reforming of methane over Ni / CeZrO2 catalysts: in-situ Studies with XRD, XAFS and AP-XPS. ACS Catal 10:3274–3284. https://doi.org/10.1021/acscatal.9b04451

[7] Sengupta S, Deo G (2015) Modifying alumina with CaO or MgO in supported Ni and Ni-Co catalysts and its effect on dry reforming of CH4. J CO2 Util 10:67–77. https://doi.org/10.1016/j.jcou.2015.04.003

[8] Safavinia B, Wang Y, Jiang C et al (2020) Enhancing Ce_x-$Zr_{1-x}O_2$ activity for methane dry reforming using subsurface Ni dopants. ACS Catal 10:4070–4079. https://doi.org/10.1021/acscatal.0c00203

[9] Xiang X, Zhao H, Yang J et al (2016) Nickel based mesoporous silica-ceria-zirconia composite for carbon dioxide reforming of methane. Appl Catal A Gen 520:140–150. https://doi.org/10.1016/j.apcata.2016.04.020

[10] Xu L, Song H, Chou L (2012) Mesoporous nanocrystalline ceria-zirconia solid solutions supported nickel based catalysts for CO_2 reforming of CH_4. Int J Hydrog Energy 37:18001–18020. https://doi.org/10.1016/j.ijhydene.2012.09.128

[11] Zhang Z, Zhang Y, Mu Z et al (2007) Synthesis and catalytic properties of $Ce_{0.6}Zr_{0.4}O_2$ solid solutions in the oxidation of soluble organic fraction from diesel engines. Appl Catal B Environ 76:335–347. https://doi.org/10.1016/j.apcatb.2007.06.011

[12] Kim JR, Myeong WJ, Ihm SK (2007) Characteristics in oxygen storage capacity of ceria-zirconia mixed oxides prepared by continuous hydrothermal synthesis in supercritical water. Appl Catal B Environ 71:57–63. https://doi.org/10.1016/j.apcatb.2006.08.015

[13] Lan L, Chen S, Zhao M et al (2014) The effect of synthesis method on the properties and catalytic performance of Pd/$Ce_{0.5}Zr_{0.5}O_2$-Al_2O_3 three-way catalyst. J Mol Catal A Chem 394:10–21. https://doi.org/10.1016/j.molcata.2014.06.032

[14] Dong XF, Zou HB, Lin WM (2006) Effect of preparation conditions of CuO-CeO_2-ZrO_2 catalyst on CO removal from hydrogen-rich gas. Int J Hydrog Energy 31:2337–2344. https://doi.org/10.1016/j.ijhydene.2006.03.006

[15] Li J, Liu X, Zhan W et al (2016) Preparation of high oxygen storage capacity and thermally stable ceria–zirconia solid solution. Catal Sci Technol 6:897–907. https://doi.org/10.1039/C5CY01571E

[16] Cao JL, Deng QF, Yuan ZY (2009) Mesoporous $Ce_{0.8}$-$Zr_{0.2}O_2$ solid solutions-supported CuO nanocatalysts for CO oxidation: a comparative study of preparation methods. J Mater Sci 44:6663–6669. https://doi.org/10.1007/s10853-009-3582-9

[17] Iglesias I, Baronetti G, Alemany L, Mari F (2018) Insight into Ni/Ce_{1-x} $Zr_xO_{2-\delta}$ support interplay for enhanced methane steam reforming. Int J Hydrog Energy 44:3668–3680. https://doi.org/10.1016/j.ijhydene.2018.12.112

[18] Wang HF, Gong XQ, Guo YLYYL et al (2009) A model to understand the oxygen vacancy formation in Zr-doped CeO_2: electrostatic interaction and structural relaxation. J Phys Chem C 113:10229–10232. https://doi.org/10.1021/jp900942a

[19] Chen HT, Chang JG (2010) Oxygen vacancy formation and migration in Ce_{1-x} Zr_xO_2 catalyst: a DFT+U calculation. J Chem Phys. https://doi.org/10.1063/1.3429314

[20] Wang HF, Li HY, Gong XQ et al (2012) Oxygen vacancy formation in CeO_2 and Ce_{1-x}Zr xO_2 solid solutions: electron localization, electrostatic potential and structural relaxation. Phys Chem Chem Phys 14:16521–16535. https://doi.org/10.1039/c2cp42220d

[21] Cao X, Zhang C, Wang Z et al (2020) Surface reduction properties of ceria-zirconia solid solutions: a first-principles study. RSC Adv 10:4664–4671. https://doi.org/10.1039/c9ra09550k

[22] Kim HJ, Jang MG, Shin D, Han JW (2020) Design of ceria catalysts for low-temperature CO oxidation. ChemCatChem 12:11–26. https://doi.org/10.1002/cctc.201901787

[23] Scanlon DO, Morgan BJ, Watson GW (2011) The origin of the enhanced oxygen storage capacity of $Ce_{1-x}(Pd/Pt)_xO_2$. Phys Chem Chem Phys 13:4279–4284. https://doi.org/10.1039/c0cp01635g

[24] Su YQ, Zhang L, Muravev V, Hensen EJM (2020) Lattice oxygen activation in transition metal doped ceria. Chin J Catal 41:977–984. https://doi.org/10.1016/S1872-2067(19)63468-6

[25] Yang Z, Woo TK, Hermansson K (2006) Effects of Zr doping on stoichiometric and reduced ceria: a first-principles

study. J Chem Phys 124:1–7. https://doi.org/10.1063/1.2200354

[26] Sun Y, Li C, Djerdj I et al (2019) Oxygen storage capacity versus catalytic activity of ceria-zirconia solid solutions in CO and HCl oxidation. Catal Sci Technol 9:2163–2172. https://doi.org/10.1039/c9cy00222g

[27] Möller R, Votsmeier M, Onder C et al (2009) Is oxygen storage in three-way catalysts an equilibrium controlled process? Appl Catal B Environ 91:30–38. https://doi.org/10.1016/j.apcatb.2009.05.003

[28] Verykios XE (2003) Catalytic dry reforming of natural gas for the production of chemicals and hydrogen. Int J Hydrog Energy 28:1045–1063. https://doi.org/10.1016/S0360-3199(02)00215-X

[29] Sengupta S, Ray K, Deo G (2014) Effects of modifying Ni/Al2O3 catalyst with cobalt on the reforming of CH4 with CO_2 and cracking of CH_4 reactions. Int J Hydrog Energy 39:11462–11472. https://doi.org/10.1016/j.ijhydene.2014.05.058

[30] Estephane J, Aouad S, Hany S et al (2015) CO_2 reforming of methane over Ni-Co/ZSM5 catalysts. aging and carbon deposition study. Int J Hydrog Energy 40:9201–9208. https://doi.org/10.1016/j.ijhydene.2015.05.147

[31] Usman M, Wan Daud WMA, Abbas HF (2015) Dry reforming of methane: Influence of process parameters—a review. Renew Sustain Energy Rev 45:710–744. https://doi.org/10.1016/j.rser.2015.02.026

[32] Perdew JP, Burke K, Ernzerhof M (1996) Generalized gradient approximation made simple. Phys Rev Lett 77:3865–3868. https://doi.org/10.1103/PhysRevLett.77.3865

[33] Perdew JP, Wang Y (1992) Accurate and simple analytic representation of the electron-gas correlation energy. Phys Rev B 45:244–249. https://doi.org/10.1103/PhysRevB.98.079904

[34] Clark SJ, Segall MD, Pickard CJ et al (2005) First principles methods using CASTEP. Zeitschrift fur Krist 220:567–570. https://doi.org/10.1524/zkri.220.5.567.65075

[35] Kresse G, Furthmüller J (1996) Efficiency of ab-initio total energy calculations for metals and semiconductors using a plane-wave basis set. Comput Mater Sci 6:15–50. https://doi.org/10.1016/0927-0256(96)00008-0

[36] Pastor-Pérez L, Le SE, Jones C et al (2018) Synthetic natural gas production from CO 2 over Ni-x/CeO_2 -ZrO_2 (x = Fe, Co) catalysts: Influence of promoters and space velocity. Catal Today 317:108–113. https://doi.org/10.1016/j.cattod.2017.11.035

[37] Ay H, Üner D (2015) Dry reforming of methane over CeO2 supported Ni, Co and Ni-Co catalysts. Appl Catal B Environ 179:128–138. https://doi.org/10.1016/j.apcatb.2015.05.013

[38] Goula MA, Charisiou ND, Siakavelas G et al (2017) Syngas production via the biogas dry reforming reaction over Ni supported on zirconia modified with CeO_2or La_2O_3catalysts. Int J Hydrog Energy 42:13724–13740. https://doi.org/10.1016/j.ijhydene.2016.11.196

[39] Pan Q, Peng J, Sun T et al (2014) CO_2 methanation on Ni/$Ce_{0.5}Zr_{0.5}O_2$ catalysts for the production of synthetic natural gas. Fuel Process Technol 123:166–171. https://doi.org/10.1016/j.fuproc.2014.01.004

[40] Aw MS, Osojnik Črnivec IG, Djinović P, Pintar A (2014) Strategies to enhance dry reforming of methane: synthesis of ceria-zirconia/nickel-cobalt catalysts by freeze-drying and NO calcination. Int J Hydrog Energy 39:12636–12647. https://doi.org/10.1016/j.ijhydene.2014.06.083

[41] Wang Z, Qu Z, Quan X, Wang H (2012) Selective catalytic oxidation of ammonia to nitrogen over ceria-zirconia mixed oxides. Appl Catal A Gen 411–412:131–138. https://doi.org/10.1016/j.apcata.2011.10.030

[42] Roh H, Potdar HS, Jun K et al (2004) Carbon dioxide reforming of methane over Ni incorporated into Ce–ZrO_2 catalysts. Appl Catal A, Gen 276:231–239. https://doi.org/10.1016/j.apcata.2004.08.009

[43] Wolfbeisser A, Sophiphun O, Bernardi J et al (2016) Methane dry reforming over ceria-zirconia supported Ni catalysts. Catal Today 277:234–245. https://doi.org/10.1016/j.cattod.2016.04.025

[44] Sutradhar N, Sinhamahapatra A, Pahari S et al (2011) Facile low-temperature synthesis of ceria and samarium-doped ceria nanoparticles and catalytic allylic oxidation of cyclohexene. J Phys Chem C 115:7628–7637. https://doi.org/10.1021/jp200645q

[45] Pahari SK, Pal P, Sinhamahapatra A et al (2015) Efficient oxidation of hydrocarbons over nanocrystalline $Ce_{1-x}Sm_xO_2$ (x = 0–0.1) synthesized using supercritical water. RSC Adv 5:45144–45151. https://doi.org/10.1039/c5ra05441a

[46] Su D, Ford M, Wang G (2012) Mesoporous NiO crystals with dominantly exposed 110 reactive facets for ultrafast lithium storage. Sci Rep 2:1–7. https://doi.org/10.1038/srep00924

[47] Marinho AL, Rabelo-Neto RC, Epron F, Bion N, Toniolo FS, Noronha FB (2020) Embedded Ni nanoparticles in $CeZrO_2$ as stable catalyst for dry reforming of methane. Appl Catal B Environ 268:118387. https://doi.org/10.1016/j.apcatb.2019.118387

[48] Fan MS, Abdullah AZ, Bhatia S (2010) Utilization of greenhouse gases through carbon dioxide reforming of methane over Ni-Co/MgO-ZrO_2: Preparation, characterization and activity studies. Appl Catal B Environ 100:365–377. https://doi.org/10.1016/j.apcatb.2010.08.013

[49] Roh H (2002) Highly active and stable Ni/Ce–ZrO_2 catalyst for H_2 production from methane. J Mol Catal A Chem 181:137–142. https://doi.org/10.1016/S1381-1169(01)00358-2

[50] Zheng Y, Wei Y, Li K et al (2014) Chemical-looping steam methane reforming over macroporous CeO_2-ZrO_2 solid solution: Effect of calcination temperature. Int J Hydrog Energy 39:13361–13368. https://doi.org/10.1016/j.ijhydene.2014.04.116

[51] Aribi K, Soltani Z, Ghelamallah M, Granger P (2018) Structure, morphology and reducibility of ceria-doped zirconia. J Mol Struct 1156:369–376. https://doi.org/10.1016/j.molstruc.2017.11.104

[52] Montoya JA, Romero-pascual E, Gimon C et al (2000) Methane reforming with CO_2 over Ni / ZrO_2–CeO_2 catalysts prepared by sol—gel. Catal Today 63:71–85

[53] Eltejaei H, Bozorgzadeh HR, Towfighi J, Omidkhah MR (2011) Methane dry reforming on Ni/$Ce_{0.75}Zr_{0.25}O_2$-$MgAl_2O_4$ and Ni/$Ce_{0.75}Zr_{0.25}O_{2\text{-}\gamma}$-alumina: Effects of support composition and water addition. Int J Hydrog Energy 37:4107–4118. https://doi.org/10.1016/j.ijhydene.2011.11.128

[54] Dantas SC, Escritori JC, Soares RR, Hori CE (2010) Effect of different promoters on Ni/$CeZrO_2$ catalyst for autothermal reforming and partial oxidation of methane. Chem Eng J 156:380–387. https://doi.org/10.1016/j.cej.2009.10.047

[55] Liu J, Zhao Z, Xu C, Liu J (2019) Structure, synthesis, and catalytic properties of nanosize cerium-zirconium-based solid solutions in environmental catalysis. Chin J Catal 40:1438–1487. https://doi.org/10.1016/S1872-2067(19)63400-5

[56] Wokaun A, Alxneit I (2015) Correlation between the structural characteristics, oxygen storage capacities and catalytic activities of dual-phase Zn-modified ceria nanocrystals†. Catal Sci Technol 5:3556–3567. https://doi.org/10.1039/c5cy00351b

[57] Hinuma Y, Toyao T, Kamachi T et al (2018) Density functional theory calculations of oxygen vacancy formation and subsequent molecular adsorption on oxide surfaces. J Phys Chem C 122:29435–29444. https://doi.org/10.1021/acs.jpcc.8b11279

[58] Kumar P, Sun Y, Idem RO (2007) Nickel-based ceria, zirconia, and ceria—zirconia catalytic systems for low-temperature carbon dioxide reforming of methane. Energy Fuels 21:3113–3123. https://doi.org/10.1021/ef7002409

[59] García-Diéguez M, Herrera C, Larrubia MÁ, Alemany LJ (2012) CO_2-reforming of natural gas components over a highly stable and selective NiMg/Al_2O_3 nanocatalyst. Catal Today 197:50–57. https://doi.org/10.1016/j.cattod.2012.06.019

[60] Wu Q, Chen J, Zhang J (2008) Effect of yttrium and praseodymium on properties of $Ce_{0.75}Zr_{0.25}O_2$ solid solution for CH_4-CO_2 reforming. Fuel Process Technol 89:993–999. https://doi.org/10.1016/j.fuproc.2008.03.006

[61] Makri MM, Vasiliades MA, Petallidou KC, Efstathiou AM (2016) Effect of support composition on the origin and reactivity of carbon formed during dry reforming of methane over 5wt% Ni/$Ce_{1\text{-}x}M_xO_{2\text{-}\delta}$ (M = Zr^{4+}, Pr^{3+}) catalysts. Catal Today 259:150–164. https://doi.org/10.1016/j.cattod.2015.06.010

[62] Nguyen TGH, Tran DL, Sakamoto M et al (2018) Ni-loaded (Ce, Zr)O2-δ -dispersed paper-structured catalyst for dry reforming of methane. Int J Hydrog Energy 43:4951–4960. https://doi.org/10.1016/j.ijhydene.2018.01.118

[63] Benguerba Y, Virginie M, Dumas C, Ernst B (2017) Methane dry reforming over Ni-Co/Al_2O_3: kinetic modelling in a catalytic fixed-bed reactor. Int J Chem React Eng. https://doi.org/10.1515/ijcre-2016-0170

[64] Dębek R, Motak M, Galvez ME et al (2017) Influence of Ce/Zr molar ratio on catalytic performance of hydrotalcite-derived catalysts at low temperature CO_2 methane reforming. Int J Hydrog Energy 42:23556–23567. https://doi.org/10.1016/j.ijhydene.2016.12.121